On cohesive element parameters and delamination modelling

Lu, X.; Ridha, M.; Chen, B. Y.; Tan, V. B.C.; Tay, T. E.

Important note
To cite this publication, please use the final published version (if applicable).
Please check the document version above.

On cohesive element parameters and delamination modelling

X. Lu[a,*], M. Ridha[a], B.Y. Chen[b], V.B.C. Tan[a], T.E. Tay[a]

[a] Department of Mechanical Engineering, National University of Singapore, 117576, Singapore
[b] Faculty of Aerospace Engineering, Delft University of Technology, 2629HS Delft, Netherlands

ARTICLE INFO

ABSTRACT

The cohesive element (CE) has been widely used to model delamination in laminated composites. The penalty stiffness, interfacial strength and fracture toughness are three CE parameters that often determine the accuracy of the numerical analysis by finite elements (FEs). The fracture toughness may be experimentally determined through standard fracture tests. The interfacial strength is difficult to obtain experimentally but also plays a crucial role in predictive numerical modelling. The penalty stiffness is a numerical parameter whose range of values may influence computational results. Recently, the CE has been deployed to model the initiation and propagation of delamination in composite structures where no pre-existing cracks or delamination has been assumed. The parameters are often calibrated, but comprehensive studies on the influence of CE parameters and their selection criteria remain limited in the literature. In the present paper, the effects of CE parameters on delamination modelling are systematically examined. The sensitivity of the overall progressive damage process and failure load to the assumed CE strengths and stiffness is studied based on selected examples of fracture and coupon-level tests. With varying CE strengths employed in the FE analyses, two distinct kinds of failure behaviour, namely the strength-sensitive and strength-insensitive delamination processes, have been observed, depending on the geometry and ply layups of composite materials. On the other hand, the penalty stiffness of CE mainly affects the computational efficiency and accuracy of delamination modelling. The failure mechanisms and physics behind are investigated to get better understanding on the numerical effects of CE parameters, and thus provide the selection guidelines in practical analyses.

1. Introduction

The initiation and propagation of interface delamination is one of the significant damage modes in composite structures and should be accurately modelled [1]. In finite element (FE) analysis, this is often achieved through cohesive elements (CEs) [2–6]. Based on an intrinsic cohesive zone model (CZM), the CE is characterized by a traction-separation cohesive law [7–9], allowing for representation of both initiation and evolution of the failure process. Various cohesive laws, such as linear, polynomial, trapezoidal and exponential relations, have been proposed and applied in numerical simulations [9–13]. In this paper, a bi-linear cohesive law is used (Fig. 1), in which three parameters are required, namely the penalty stiffness K_p, the cohesive strength τ^c and the fracture toughness G_c. While the penalty stiffness K_p describes the initial elastic material behaviour before damage onset, the strength τ^c reflects the maximum stress that can be sustained by the interface. The fracture toughness G_c is a well-established material property representing the resistance to crack propagation during the damage evolution (area under the traction-separation curve). Three

---

* Corresponding author.
  E-mail address: xinlu@u.nus.edu (X. Lu).

Nomenclature

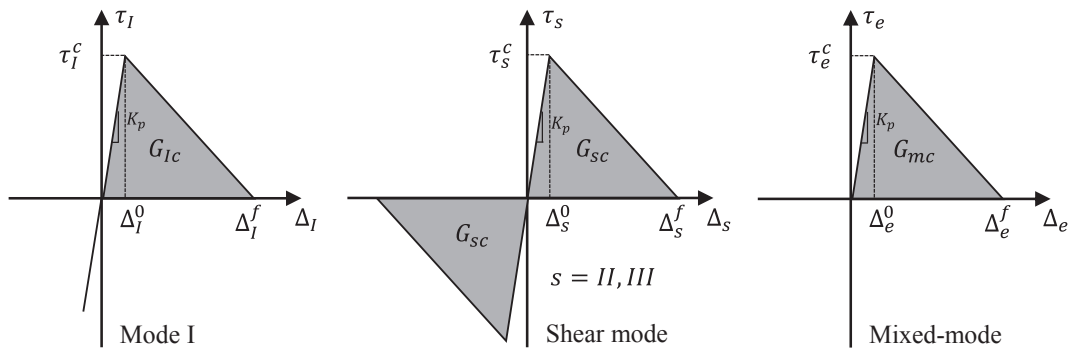|			
d_m	damage variable of cohesive zone model	Δ_i^f	mode i separation at final failure, i = I, II, III
d_m'	equilibrium damage factor of last time step	Δ_i^*	mode i separation at crack tip, i = I, II, III
$E_{(ii)}$	Young's modulus in direction i, i = 1, 2, 3	Δ_e	effective separation
$G_{(ij)}$	shear modulus in plane ij, ij = 12, 13, 23	ΔT	temperature change
G_{ic}	mode i fracture toughness, i = I, II, III	ν_{ij}	Poisson's ratio in plane ij, ij = 12, 13, 23
G_{mc}	mixed-mode fracture toughness	τ	traction vector
J	J integral	τ_i	mode i traction, i = I, II, III
K_p	penalty stiffness	τ_i^c	mode i interface strength, i = I, II, III
S_l	in-plane longitudinal shear strength	τ_e	effective traction
Y_t	in-plane tensile strength	B-K	Benzeggagh–Kenane
α	power law coefficient	CE	cohesive element
α_{ii}	coefficient of thermal expansion in direction i, i = 1, 2, 3	CZM	cohesive zone model
		DCB(M)	(modified) double cantilever beam
η	Benzeggagh–Kenane law coefficient	ENF(M)	(modified) end-notched flexure
Γ	integration path around crack tip	FE	finite element
Γ_t	integration path close to crack tip	MMB	mixed-mode bending
Δ	separation vector	OHC	open-hole compression
Δ_i	mode i separation, i = I, II, III	OHT	open-hole tension
Δ_i^0	mode i separation at failure onset, i = I, II, III	SI	static indentation

Fig. 1. The traction-separation cohesive law for CE formulation.

individual fracture modes and their mixity, i.e., mode I, mode II, mode III and mixed-mode, are considered to describe the fracture failure under general loading conditions. In most applications, the value of the mode III fracture toughness is often assumed to be the same as the mode II toughness. The fracture toughness of different failure modes can be obtained experimentally through standardized tests, such as the double cantilever beam (DCB, mode I), end-notched flexure (ENF, mode II) and mixed-mode bending (MMB, mixed-mode) [14–17], whereas no standard tests are available for measurement of interfacial strengths and the penalty stiffness is a non-physical numerical parameter. Compared to the fracture toughness, it is less straightforward to determine these two parameters (τ^c and K_p) for FE modelling.

Cohesive strengths directly determine the failure onset and the subsequent material softening process. The relationship between cohesive strength and mesh size has been widely researched in the literature [18–22]. Accurate modelling of delamination propagation requires very fine mesh along the potential crack path [23–25], but adopting reduced interfacial strengths could mitigate such excessive mesh size requirement to some extent [19]. Nonetheless, as reported by Harper et al. [26], in some cases the artificially reduced cohesive strength may have unintended effects on numerical results due to its influence on cohesive zone length, mode mixity and energy dissipation.

Although the penalty stiffness is a numerical parameter used to maintain connection between the plies prior to delamination initiation [27–29], it is significant and often necessary in FE modelling [30]. An appropriate value of K_p must be selected such that it should not be too low to alter the overall compliance of the structure nor too high to trigger non-convergence [19]. However, within the allowable range considering both numerical accuracy and feasibility, various K_p values have been found to affect numerical predictions [30–32], especially under mixed-mode loading [33–35].

Most sensitivity studies of CE parameters in literature are performed on standard fracture toughness tests, i.e. DCB and ENF specimens. However, increasingly CEs are employed in other structural models to predict delamination damage of composite structures. The open-hole tension (OHT) [36–38], open-hole compression (OHC) [39,40], impact-damaged [41,42] composite laminates, etc., have been extensively modelled with CEs. The question whether calibrations of parameters from analyses with pre-

cracks such as the DCB and ENF can be directly applied without modification to structural-level models remains valid and important.

In this paper, a comprehensive study on effects of CE parameters under various boundary and loading conditions is presented. The FE modelling is performed with Abaqus Implicit (version 6.14) under quasi-static loading, and the sensitivity of delamination damage to the cohesive strength and penalty stiffness is examined. Significant variations in the sensitivity of the CE strengths are observed when different cases with constant penalty stiffness are analysed, and failure behaviour can be divided into two distinct categories, namely strength-insensitive and strength-sensitive. On the other hand, the CE penalty stiffness generally affects overall computational efficiency. While excessively low penalty stiffness leads to inaccurate predictions due to increase in structural compliance, CE models with overly high stiffness increase the number of iterations and may not achieve convergence.

In Section 2, the background of CZM and formulation of CE are briefly reviewed. Numerical parametric studies of CE strength and penalty stiffness are presented in Sections 3 and 4, respectively. Finally, conclusions are drawn in Section 5.

2. Cohesive zone model and cohesive element

The fundamentals of CZM and CE formulation [3,9] are briefly introduced. The tractions acting on an interface modelled with CEs are given by:

$$\tau_i = (1 - d_m)K_p\Delta_i, \ i = I, \ II \ \ and \ \ III, \tag{1}$$

where τ_i and Δ_i are the components of traction vector τ and separation vector Δ respectively, and $i = I, \ II \ \ and \ \ III$ denote the three modes of loading. d_m is the damage factor characterizing the irreversible damage process, with $d_m = 0$ and $d_m = 1$ representing the intact and fully failed states, respectively.

Delamination onset is frequently predicted by the quadratic criterion [29,43]:

$$\left(\frac{\tau_I}{\tau_I^c}\right)^2 + \left(\frac{\tau_{II}}{\tau_{II}^c}\right)^2 + \left(\frac{\tau_{III}}{\tau_{III}^c}\right)^2 = 1, \tag{2}$$

where τ_i^c represents the strength for mode i failure ($i = I, \ II \ \ and \ \ III$). As shown in Fig. 1, the damage evolution popularly follows a mixed-mode bilinear cohesive law [29], although expressions other than bilinear may also be used:

$$\int_0^{\Delta_e^f} \tau_e d\Delta_e = \frac{1}{2}\tau_e^c \Delta_e^f = G_{mc}, \tag{3}$$

in which

$$\Delta_e = \sqrt{\langle\Delta_I\rangle^2 + \Delta_{II}^2 + \Delta_{III}^2},$$
$$\tau_e = \frac{(\tau_I\langle\Delta_I\rangle + \tau_{II}\Delta_{II} + \tau_{III}\Delta_{III})}{\Delta_e},$$
$$\langle\Delta_I\rangle = \max(0, \Delta_I). \tag{4}$$

G_{mc} is the mixed-mode fracture toughness, which is sometimes determined by either the B-K law [44]:

$$G_{mc} = G_{Ic} + (G_{IIc} - G_{Ic})\left(\frac{G_{II}}{G_I + G_{II}}\right)^\eta; \tag{5}$$

or power law [29]:

$$G_{mc} = \left[\left(\frac{\lambda_I}{G_{Ic}}\right)^\alpha + \left(\frac{\lambda_{II}}{G_{IIc}}\right)^\alpha + \left(\frac{\lambda_{III}}{G_{IIIc}}\right)^\alpha\right]^{-1/\alpha}, \tag{6}$$

where η and α are the B-K law and power law coefficient, respectively. $G_i = 1/2\tau_i\Delta_i$ (no summation) and $\lambda_i = G_i/\sum_j G_j$ are determined at failure onset.

The damage factor d_m determining failure progression is calculated based on current deformation and the damage history:
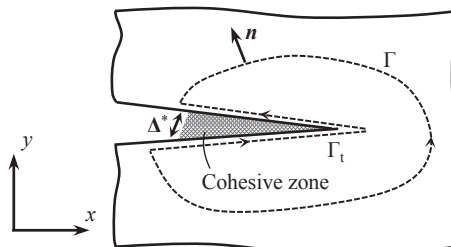

Fig. 2. The cohesive zone and path-independent J integral in an arbitrary contour Γ.

$$d_m = \max\left[\frac{\Delta_e^f(\Delta_e - \Delta_e^0)}{\Delta_e(\Delta_e^f - \Delta_e^0)}, d_m'\right],$$

(7)

where d_m' is the equilibrium damage factor from the previous loading step.

3. Strength of a cohesive element

In this section, the influence of the CE strength parameters in delamination modelling of composite laminates is studied. According to the stress-based failure criterion of Eq. (2), the normal and shear interfacial strengths directly govern failure initiation at the material interface [45]. While it is relatively straightforward to obtain the intralaminar tensile and shear strengths through testing unidirectional laminates [46–48], there is no direct method to obtain interfacial strengths.

Alternatively, the cohesive law and associated cohesive strengths may be determined through the path independent J integral based on linear elastic fracture mechanics (LEFM) in Fig. 2 [49,50]. Taking the arbitrary path Γ close to the crack tip, the integral path may be reduced to Γ_t and the traction-separation relationship of the crack surfaces may be derived [51–55]:

$$\tau_i = \frac{\partial J}{\partial \Delta_i^*}, \quad i = I, II \quad and \quad III,$$

(8)

in which Δ_i^* is the mode i crack-tip openings (Fig. 2). By continuously measuring the crack-tip opening at the end of the cohesive zone and J integral (R-curve) in the experiments, the cohesive law can be evaluated through Eq. (8) [56–59].

The LEFM method has been widely adopted to analyse the fracture behaviour of adhesive joints in composites [55–58]. Although Eq. (8) provides a means to determine the apparent strengths of interfaces, in practice, the delamination can initiate and propagate rapidly, so that it becomes difficult to accurately measure the crack-tip opening. For this reason, the assumed values for interfacial strengths are usually adopted in numerical simulations and in many cases, they are set to be the same as in-plane intralaminar strengths [60–65]. Nonetheless, a few studies suggest that that such assumption could lead to inaccurate predictions of the structural failure behaviour [66]; therefore adjusted strength values are sometimes adopted to achieve better correlation with experimental results [67–73]. On the other hand, reduced strengths are also sometimes used to improve computational efficiency for the fracture propagation, e.g., specimens with pre-cracks [74].

Table 1
Literature review on the material parameters applied in numerical modelling for various carbon/epoxy systems under different loading conditions.

Ref.	Material	Simulation	In-plane strength Y_t/S_l (MPa)	Interface strength τ_I^c/τ_{II}^c (MPa)	K_p (N/mm³)
Turon [45]	AS4/PEEK	DT	–	80/100	10^6
Harper [20]	HTA6376/C	DT	–	30/60	10^5
Soto [21]	T300/977-2	DT	–	60/80	10^6
Dávila [75]	IM6/3501-6	DT	–	61/68	–
Hallett [61]	IM7/8552	OHT	60/90	60/90	–
Higuchi [37]; Camanho [76]	IM7/8552	OHT	62.3/92.3	62.3/92.3	–
Ridha [38]	IM7/8552	OHT	62.3/81.5	62.3/81.5	10^6
Swindeman [77]	IM7/8552	OHT	76/90	76/90	2.71×10^8
Lu [71]; Van Der Meer [67]	IM7/8552	OHT	60/90	<u>30/45</u>	10^6
Chen [69,70]	IM7/8552	OHT	60/90	<u>40/50</u>	10^6
Wang [78]	IM7/5250	OHT	66/103	66/103	–
Zhou [79]	Hexcel F593	OHT	98/40	98/40	–
De Carvalho [80]	IM7/8552	DM	64–127/112–223	64–127/112–223	–
Chen [81]; Lu [25]; Hu [82]	IM7/8552	DM	60/90	60/90	1.6×10^5
Ling [83]	IM7/8552	DM	80/90	80/90	–
Hu [84]	T700/-	DM	40/50	40/50	–
Tay [85]	AS4/3501-6	DM	57/75	<u>60/68</u>	–
Soto [86]	AS4/8552	Impact	26/78.4	26/78.4	2.5×10^4
Sun [65]	IM7/8552	Impact	60/90	60/90	–
McElroy [87]	IM7/8552	Impact	129/93	129/93	–
Bouvet [88]	T700/M21	Impact	50/90	50/90	10^6
Hongkarnjanakul [41]	T700/M21	Impact	60/110	60/110	–
Abir [42]	T700/M21	Impact	75/150	75/150	10^6
Zhi [73]	Hexcel 913C	Impact	60/–	<u>105/105</u>	10^6
Su [39]	IM7/8552	OHC	60/90	<u>40/50</u>	–
Zhou [89]	IM7/8552	OHC	60/90	<u>62.3/81.5</u>	–
Hoos [90]	IM7/977-3	OHT/OHC	100/100(80)	100/100(80)	–
Falcó [40]	AS4/8552	OHT/OHC	74.2/110.4	74.2/110.4	–
Yang [91]	IM7/8551	TT	73/92	<u>–/92</u>	–
Yang [91]	IM7/3501	TT	57/72	<u>–/78</u>	–
Iarve [63]	T300/976	TT	37.9/100	37.9/100	–

DT: delamination test; OHT: open-hole tension; DM: delamination migration; OHC: open-hole compression; TT: tensile test.
Underline: interface strengths are different from the in-plane strengths.

3.1. Selection of the CE properties in numerical modelling

A review of recent papers lists the material properties for carbon/epoxy composite laminates used in FE analyses in Table 1 for various cases involving delamination analysis, open-hole tension/compression (OHT/OHC), delamination migration (DM), impact and tensile tests.

For the modelling of standard fracture toughness tests, CE strength values have very limited influence on the predicted results [74], and thus assumed interface strengths can be applied. On the other hand, interface strengths may be significant when more complex composite structures are analysed. Table 1 shows that different strength values have been applied in the CE modelling even for the same material system. For example, various cohesive strength values have been assumed for IM7/8552 composite laminates, τ_I^c from 30 MPa to 127 MPa and τ_{II}^c from 45 MPa to 223 MPa by different research groups. De Carvalho et al. [80] performed a strength sensitivity study on the DM modelling and more accurate predictions were achieved with higher strengths (127/223 MPa) as compared to the normally used values (60/90 MPa). A calibration process of material properties was conducted by Hoos et al. [90] after the blind prediction stage, in which the shear strength was reduced from 100 MPa to 80 MPa to get better prediction on crack initiation. Reduced interfacial strengths have also been adopted by Lu et al. [71], Van Der Meer et al. [67] and Chen et al. [69,70] to achieve better agreement with experimental results (Table 1).

The following sections present parametric studies on the influence of cohesive strengths on analysis of several loading cases. Sections 3.2–3.4 discuss analysis of delamination tests, i.e. DCB, ENF, etc., while Sections 3.5 and 3.6 discuss coupon level analysis.

3.2. Double cantilever beam (DCB) and end-notched flexure (ENF) tests

As shown in Fig. 3, FE analyses on DCB and ENF [4,18] are performed. The dimensions of the beam are length $2L = 100$ mm, thickness $h = 3$ mm. The width is 20 mm for DCB and 1 mm for ENF in the numerical examples. For both DCB and ENF, a pre-crack of length $a = 30$ mm is modelled and the material properties are given in Table 2. CEs are pre-located along the potential crack path and prescribed displacements Δ are applied. Four-node plane stress quadrilateral elements are adopted to model the solid beams and three elements are used through the thickness. Small deformation and geometric linear analysis are applied.

The dependence of the predicted maximum load (structural strength) on the CE element size is shown for both DCB and ENF tests in Fig. 4a-b. Apart from the interfacial strengths provided in the literature (Table 2), a range of strength values, i.e., from 1 to 200 MPa, are used to test the sensitivity of the results. Coarse meshes may cause significant over-predictions of the maximum load, but the results converge to the analytical solution [14] with modest mesh refinement. Higher CE strengths lead to finer mesh requirement for convergence, and as shown in [19], adopting reduced strength values allows use of relatively coarse CE meshes. Note that lower CE strengths imply larger cohesive zones with smoother stress gradients [20,92].

However, when the mesh is sufficiently fine (e.g., 0.1 mm for both DCB and ENF), the predicted maximum loads are generally insensitive to the assumed CE strengths (Fig. 4c and d). However, given an extremely high $\tau_I^c = 200$ MPa in the DCB analysis (Fig. 4c), even the 0.1 mm mesh is insufficiently fine and results in over-predictions of the peak load and subsequent softening curve. With further mesh refinement (labelled "200 MPa (0.05 mm)" in Fig. 4c), the results converge with the other curves. In contrast, with excessively low strength values, i.e., 1 MPa for both cases, the interface failure initiates at very low loading levels, resulting in premature non-linear behaviour (Fig. 4c and d). Except for these extremely high and low CE strengths, the predicted delamination onset and propagation compare well with the reference analytical solution. It can be concluded that the fracture of DCB and ENF specimens are strength-insensitive.

To further investigate the effects of CE strength in delamination modelling, the analyses are repeated without pre-cracks in the DCB and ENF but with the same geometry and material properties; these are labelled the modified double cantilever beam (DCBM) and end-notched flexure (ENFM) (Fig. 5). As in the DCB and ENF simulations, CEs are inserted along the interface at the mid-plane, where the initiation and progression of delamination is anticipated.

The numerical results of DCBM and ENFM tests are provided in Fig. 6. Unlike the standard DCB and ENF analyses, the predicted strengths are less sensitive to CE size (Fig. 6a and b). However, the maximum predicted loads show a strong dependence on the assumed CE strengths. Unstable delamination propagation occurs right after failure onset, leading to significant load drops as shown
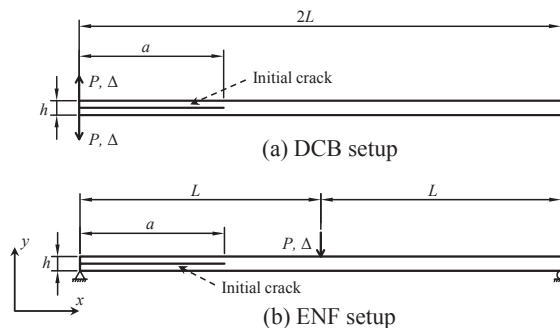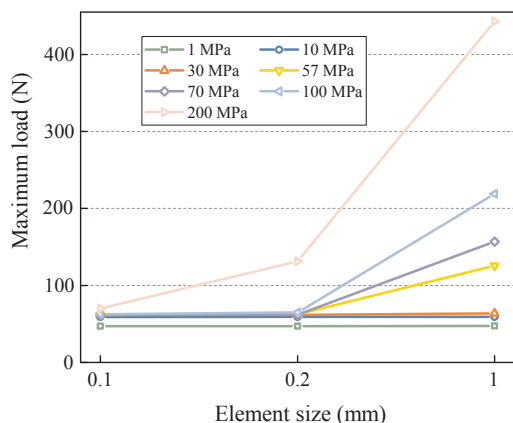

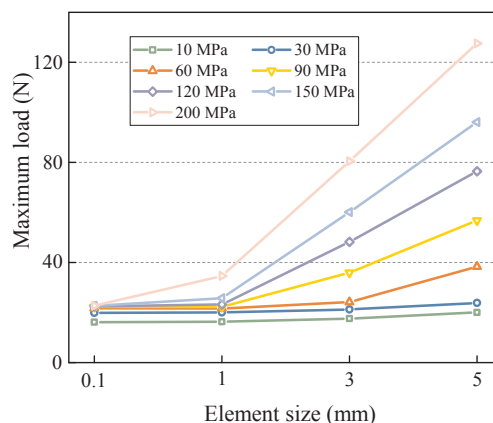Fig. 3. Setups for double cantilever beam (DCB) and end-notched flexure (ENF) tests.

Table 2

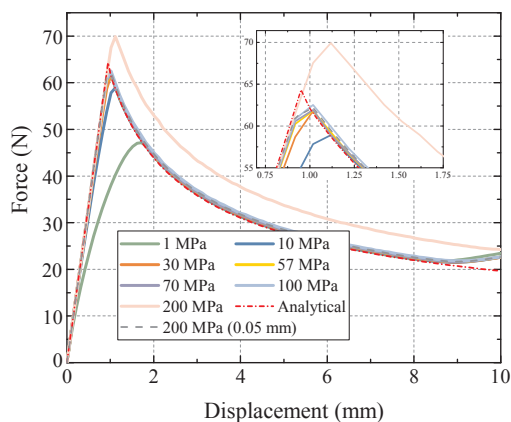Homogenized material properties for the DCB and ENF models [18].

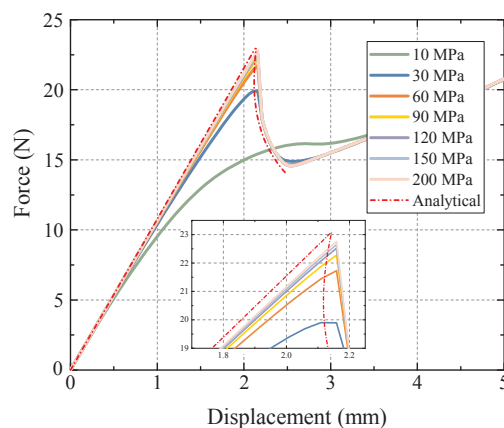| E_{11} (GPa)	E_{22}/E_{33} (GPa)	G_{12}/G_{13} (GPa)	G_{23} (GPa)	ν_{12}/ν_{13} (–)	G_{Ic}/G_{IIc} (N/mm)	τ_I^f/τ_{II}^f (MPa)	K_p (N/mm^3)
135.3	9	5.2	3.08	0.24	0.28/0.63	57/90	10^6

(a) Mesh sensitivity of DCB test.

(b) Mesh sensitivity of ENF test.

(c) Load-displacement curves of DCB test (0.1mm mesh).

(d) Load-displacement curves of ENF test (0.1mm mesh).

Fig. 4. Numerical results of DCB and ENF tests with different CE element sizes and interfacial strengths.

(a) DCBM setup

(b) ENFM setup
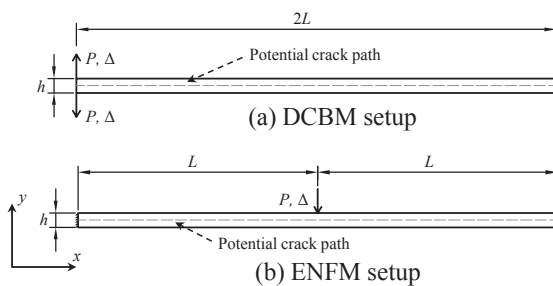
Fig. 5. Setups for modified double cantilever beam (DCBM) and modified end-notched flexure (ENFM) tests without pre-cracks.

(a) Mesh sensitivity of DCBM test.

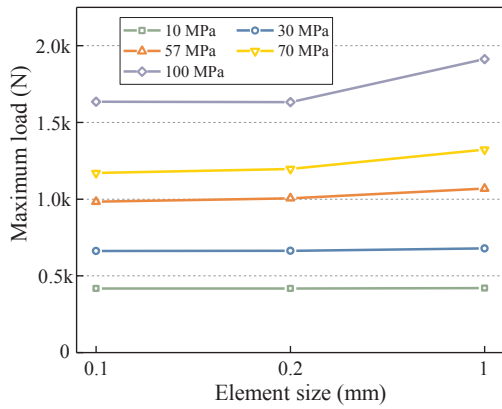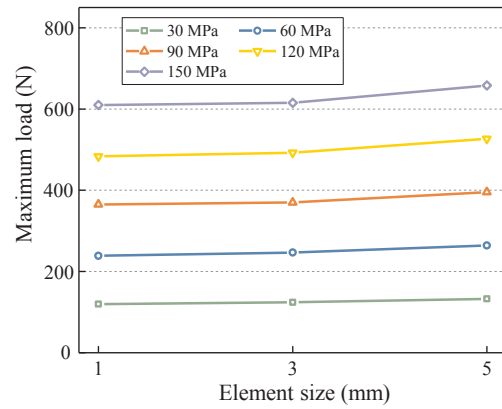(b) Mesh sensitivity of ENFM test.

(c) Load-displacement curves of

DCBM test (0.1mm mesh).
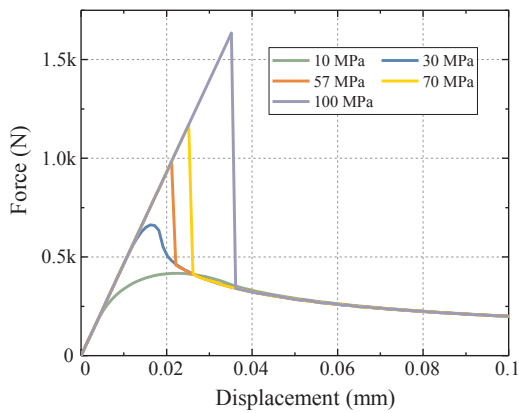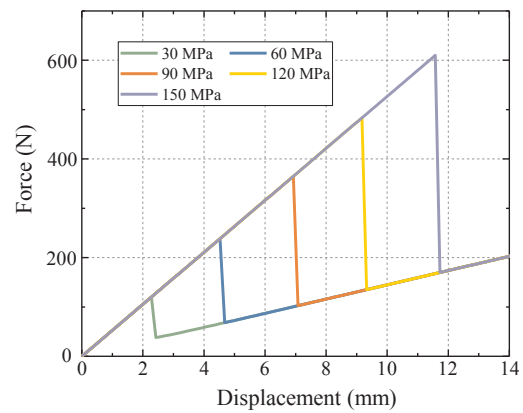
(d) Load-displacement curves of

ENFM test (1mm mesh).

Fig. 6. Numerical results of DCBM and ENFM tests with different mesh sizes and interfacial strengths.

in Fig. 6c and d. Without pre-cracks embedded in the DCBM and ENFM specimens, the fracture process becomes highly strength-sensitive.

Remark 1 (_Comparison between the standard and modified fracture toughness specimens_**).** Although the use of CEs avoids dealing directly
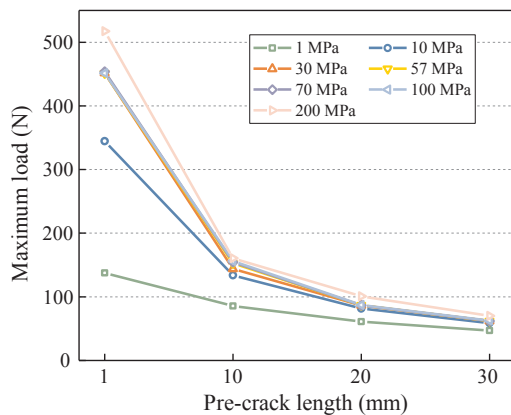
(a) DCB test with different pre-crack lengths. (b) ENF test with different pre-crack lengths.
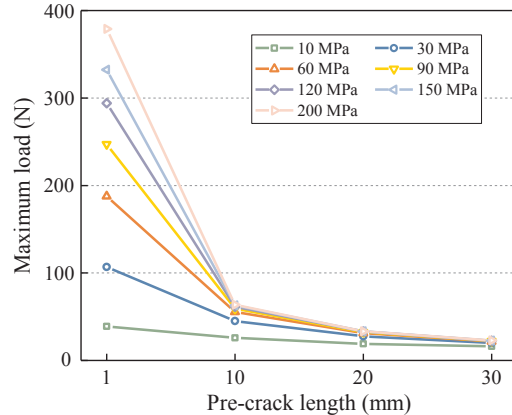
Fig. 7. The effects of pre-crack lengths in DCB and ENF tests.

with the stress singularity at crack tip and the singular stress is effectively smeared within the cohesive zone, high stress concentration still exists when a pre-delamination is defined in the model, easily triggering the failure of the interface CEs. Thus, the overall failure behaviour of DCB and ENF is not sensitive to the interfacial strengths. In contrast, without very high stress concentrators in the DCBM and ENFM, the failure is governed by the assumed CE strengths.

Remark 2 (*Effects of the pre-crack lengths*). As shown in Fig. 7, the influence of CE strengths is only significant for rather short pre-cracks, and this effect is more pronounced for ENF than DCB.

3.3. Free-edge delamination

Free-edge delamination is analysed in this sub-section. Without pre-existing cracks, free-edge delamination is a typical failure mode in composite laminates, which has been extensively researched in the literature [93–96]. Due to the mismatch in fibre orientations and orthotropy of the composite lamina, high stress exists at the free edges, triggering the initiation of delamination [93–96]. In the numerical model shown in Fig. 8 where $h = 0.792$ mm and $b = 25$ mm, the $[25/-25/90]_s$ composite laminate is subjected to a tensile load along the x-axis and the edge delamination occurs at the 90°/90° interface due to the high tractions through the thickness [19]. The cross-section of the laminate is modelled with generalized plane strain elements, and CEs are inserted along the 90°/90° interface where the onset and growth of delamination are expected. No pre-cracks are defined in the model. The material properties adopted in the analyses are provided in Table 3.

As shown in Fig. 9a, extremely fine meshes are required to obtain converged results and such requirement keeps increasing if higher CE strengths are adopted. With different assumed CE strengths employed in the numerical models, the predicted maximum loads turn out to be similar to each other given a sufficiently fine mesh, implying a strength-insensitive failure process. The load-displacement curves (Fig. 9b) show that for a fine mesh, i.e. 0.02 mm, the maximum loads are in close agreement with experimental result [19], regardless of assumed CE strengths. Although applying excessively low or high strength values (e.g., either 1 or 150 MPa) may cause fluctuation in the predicted failure stresses, the numerical errors are within 7% as compared to the experimental result. In addition, slight nonlinearity in the loading curves is observed when relatively low interface strengths are adopted, indicating delamination propagation prior to abrupt load drop.

It should be noted that unlike in the DCB or ENF models, the free-edge delamination models do not contain any pre-cracks. The failure behaviour is, however, driven by the crack-like high stress concentration along the 90°/90° interface before the load drop (Fig. 9c), which exhibits great similarity to the stress fields in DCB and ENF when they are modelled with CEs (Remark 1). This means that the free-edge delamination behaves similarly to the DCB and ENF models, where the results are not sensitive to the assumed CE strengths, as long as the mesh size is fine enough.

3.4. Stiffener debonding

Skin/stiffener debonding is a typical delamination problem for which modelling by CEs are well suited [75]. Different configurations of the stiffener flanges (Fig. 10) affect the mechanical performance [97]. The straight and tapered stiffener flanges are modelled with dimensions $h_1 = 2$ mm, $h_2 = 1.8$ mm, $b_1 = 120$ mm, $b_2 = 45$ mm and $b_3 = 30$ mm. Three-point bending loads are applied and the assumed material properties are shown in Table 2.

There are significant differences between the straight and tapered flanges when stiffener debonding is modelled in the analyses (Fig. 11). For the specimens with straight flanges, the predicted delamination process is not sensitive to the CE strengths, and consistent results are obtained with a wide range of interfacial strength values (Fig. 11a). However, if tapered flanges are used, the overall failure becomes strength-sensitive and relies significantly on the input strength values (Fig. 11b). This is similar to the results
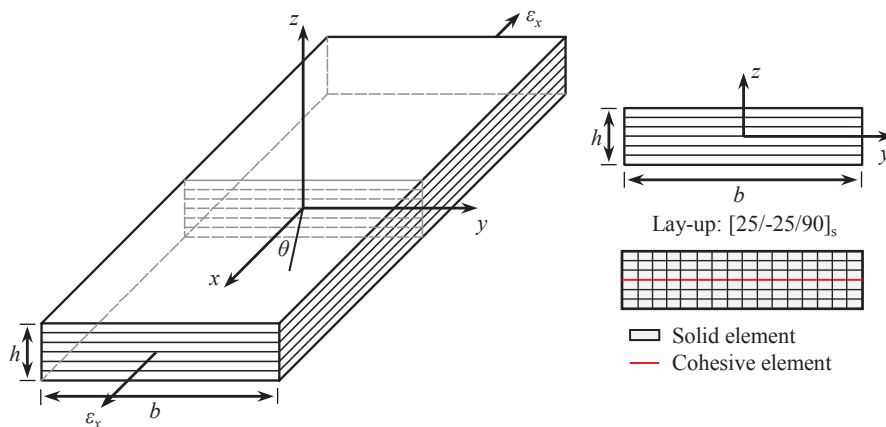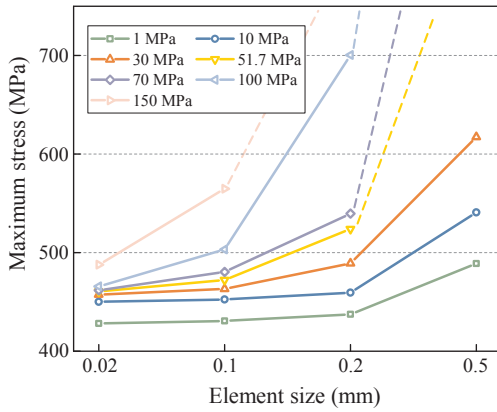

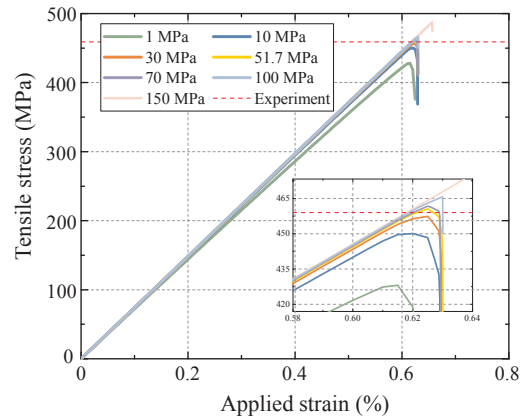Fig. 8. Free-edge delamination problem.

Table 3
Material properties of T300/934 graphite-epoxy for the free-edge delamination analyses [19].

E_{11} (GPa)	E_{22}/E_{33} (GPa)	G_{12}/G_{13} (GPa)	G_{23} (GPa)	v_{12}/v_{13} (–)	v_{23} (–)	G_{Ic} (N/mm)	τ_I^c (MPa)	K_p (N/mm^3)
140	11	5.5	3.61	0.29	0.4[*]	0.175	51.7	10^6

  * Assumed values.

(a) Mesh sensitivity of free-edge delamination analysis.

(b) Load-displacement curves (0.02mm mesh).
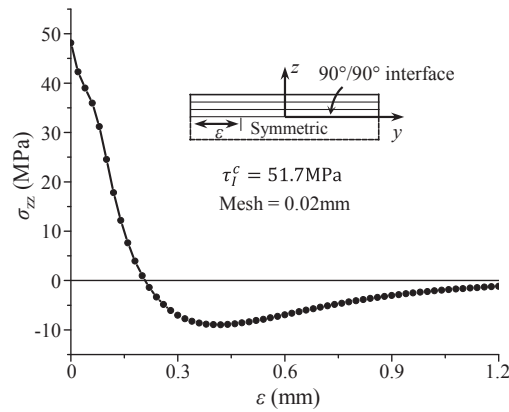
(c) Normal stress at 90°/90° interface before the load drop.

Fig. 9. Numerical results of free-edge delamination analyses.

(a) Straight flange

(b) Tapered flange
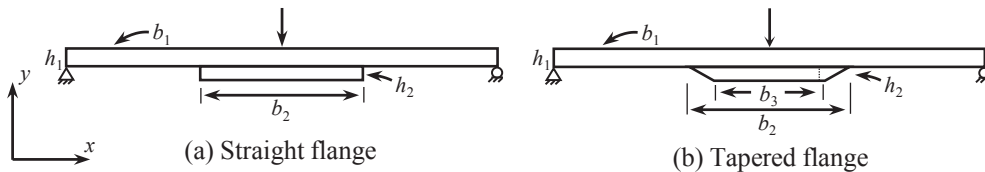
Fig. 10. Geometry and boundary conditions for stiffener debonding tests.

of the DCBM and ENFM without pre-cracks.

In the composite structures with straight flanges, prominent stress concentrations exist at the corners of the specimen due to the rapid geometry change (Fig. 11c). The localized high stresses resemble the crack-tip high stress gradients and this accounts for the insensitivity of debonding process to the interface strengths. For the tapered flanges, the stress concentrators at the edges of the flange are effectively eliminated (Fig. 11d), resulting in dependence on CE strengths.

(a) Mesh sensitivity of straight flange test.

(b) Mesh sensitivity of tapered flanges.

(c) Load-displacement of straight flange (0.1mm mesh).

(d) Load-displacement of tapered flange (0.1mm mesh).

Fig. 11. Numerical results of stiffener debonding analyses.

Remark 3. From the above, it is the crack-like high stress concentrators that dominate the fracture behaviour and the presence or modelling of pre-cracks is not always necessary, as illustrated by the free-edge delamination and skin-stiffener d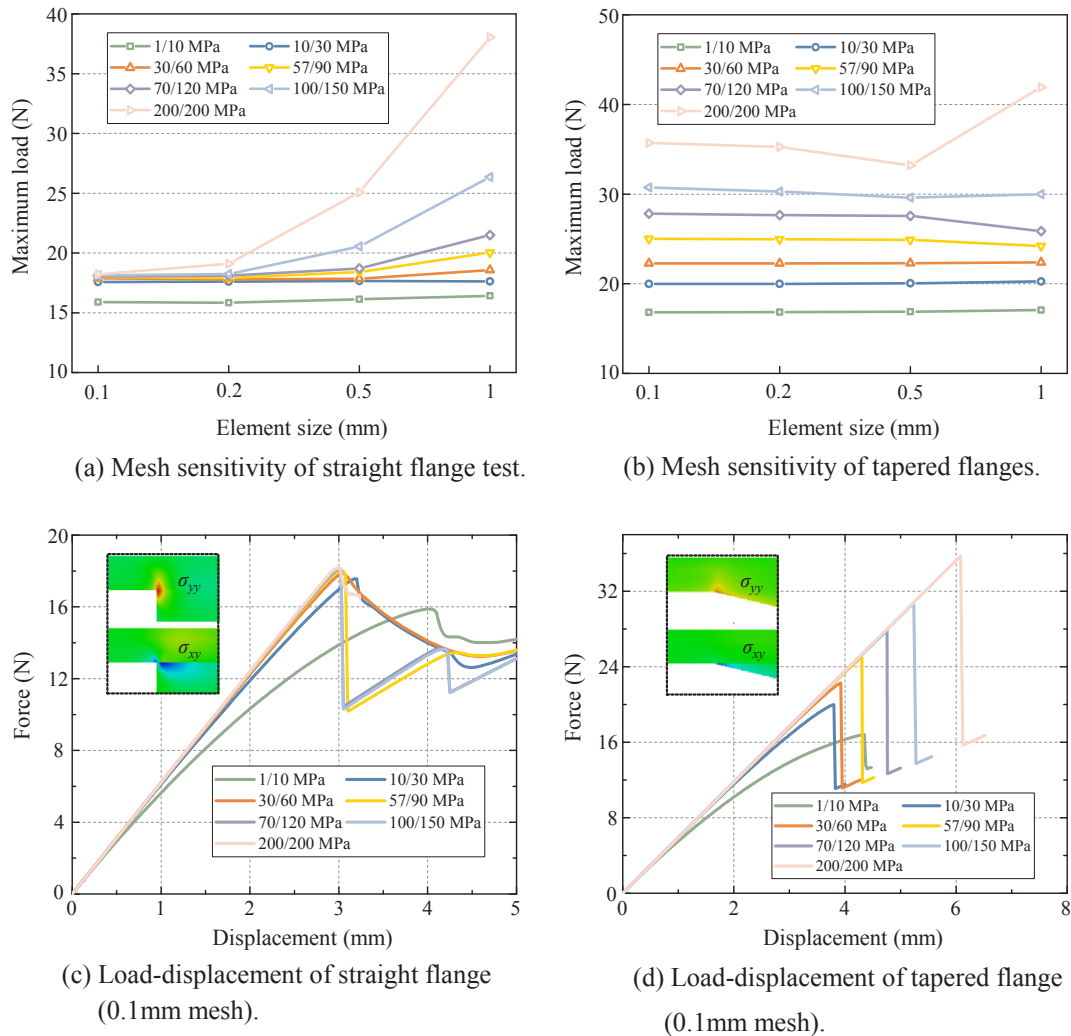ebonding problems. Furthermore, for strength-insensitive fracture with crack-like stress concentrations, excessively fine mesh is required for converged predictions and it is acceptable to use reduced CE strengths for application with larger CEs, as reported by Turon et al. [19].

3.5. Structural damage analyses: open-hole tension (OHT) test

The numerical examples provided in Sections 3.2–3.4 are two-dimensional problems for which only a single delamination is modelled. However, in composite laminates with dissimilar fibre orientations, multiple delaminations may occur concurrently at different interfaces, and the interaction between matrix cracking and interface delamination should be considered. To ensure the reliability of numerical modelling for practical applications, it is important to understand the influence of the interfacial strengths in
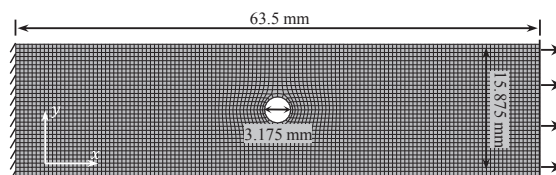

Fig. 12. FE mesh (0.5 mm) and boundary conditions for open-hole tension (OHT) tests.

structure- and coupon-level analyses. In the current and following sections, open-hole tension (OHT) and static indentation (SI) tests are modelled and analysed to study the effects of assumed CE strengths.

The OHT on $[45_4/90_4/-45_4/0_4]_s$ IM7/8552 composite laminate in [61,98] is modelled as shown in Fig. 12 and the material properties used in the simulations are given in Table 4. Both matrix cracking and interface delamination are simulated with the floating node method [70]. As summarized in Table 1, various interlaminar strength values for IM7/8552 have been used in literature. In the present study, the strengths of interface are first assumed to be the same as those of ply materials, i.e. 60/90 MPa, as commonly adopted by researchers [61,63]. The effect of other assumed CE strengths is also examined. Three meshes (0.2 mm, 0.5 mm and 1 mm) are used, and a minimum 1.5 mm crack spacing is specified for all the models [36,81].

Experimental results from Hallett et al. [61] showed that the failure of OHT $[45_4/90_4/-45_4/0_4]_s$ laminates was primarily delamination dominated, in which extensive interfacial damage occurs between dissimilar plies. The widely-spread delamination, particularly at $-45°/0°$ interface, led to load-drop and loss of structural stiffness. In this delamination failure mode, they defined failure strength as the stress at the load-drop caused by delamination propagation [61]. Fig. 13 shows the failure strength predicted by the models with different CE strengths and mesh sizes. Although noticeable variations are obtained in the predicted structural failure strengths, the delamination failure patterns of individual models right after load-drop do not differ much when different CE strengths are employed, as plotted in Fig. 14. Unlike the other previous cases, failure of OHT specimens consists of multiple delamination propagations at different interfaces and the interaction between matrix cracking and interface delamination may not be ignored. The two coupled failure mechanisms are intensively affected by selection of the element sizes and CE strengths. According to Fig. 13, significant reduction in the failure strength is observed if smaller element sizes and lower CE strengths are adopted, indicating strength-sensitive behaviour. Mesh convergence on strength prediction is generally observed for models with relatively high interface strengths, i.e., 40/60 MPa and higher values. However, when lower CE strengths (20/30 MPa and 30/45 MPa) are assumed, the mesh convergence is not obtained even after the mesh is refined to 0.2 mm. This problem also occurs on the predictions of interfacial damage (Fig. 15). Under the same applied displacement, models with higher strength values (i.e., 60/90 MPa and 90/135 MPa in Fig. 15) tend to provide converged results. In contrast, such a converged trend does not exist when the overly low 20/30 MPa strengths are adopted, in which larger damaged area are predicted with finer mesh (Fig. 15). With low strengths, CEs can easily start to fail and their failure initiation is largely affected by the resolution of calculated stress concentration at the delamination front which is very sensitive to the mesh size. For the finest 0.2 mm mesh, more CEs fail at early loads, thus resulting in the significant softening responses and lower predicted failure strengths.

The distribution of the average traction, $\tau_{avg} = \sqrt{\langle\tau_I\rangle^2 + \tau_{II}^2 + \tau_{III}^2}$, at $-45°/0°$ interface is shown in Fig. 16a. For the intact CE interface, high tractions are observed around the notch edge. However, with the emergence of matrix cracks which further triggers the initiation of delamination damage (Fig. 16b), such localized stress concentrations are gradually replaced by larger high-traction regions (middle and right figures). Consequently, the effects of local stress concentrators are significantly alleviated and the delamination failure process is mainly determined by the overall loading capability of the interface. This accounts for the strength sensitivity of the OHT model. It is noted that if the ply material strengths assume lower values of 30/45 MPa, there is better agreement with experimental results but this could be fortuitous.

3.6. Structural damage analyses: static indentation (SI) test

A static indentation (SI) analysis is performed on a $[0_2/45_2/90_2/-45_2]_s$ T700/M21 laminate (Table 5) and the model details are shown in Fig. 17. Hexahedral continuum shell elements (SC8R) are employed for each composite layer while CEs are placed between plies to model delamination. A common prescribed displacement of 1.0 mm in the z-direction is imposed on the indenter; three models, a coarse mesh with 1×1 mm elements, a fine mesh with 0.5×0.5 mm elements and further refined mesh with 0.25×0.25 mm elements, are constructed in the mid-region of the plate around the impact area. Only delamination failure is simulated (no in-plane damage) in the model. Similar to the OHT analyses, four groups of interfacial strengths, i.e. 20/37 MPa, 30/55 MPa, 60/110 MPa and 90/165 MPa, are tested in the simulations.

Based on the mesh sensitivity study (Fig. 18), FE mesh with 1×1 mm elements is too coarse to achieve converged results, particular when higher CE strengths are adopted. Convergence of results is achieved with the 0.5 mm × 0.5 mm as well as the 0.25×0.25 mm meshes. Although various CE sizes and strengths are used in the FE models, the load-displacement response, i.e., the overall compliance of the laminate remains similar [99]. As shown in Fig. 18, the maximum indenter force increases slightly from 2082 N to 2302 N with increase of element size and interface strengths. However, the predicted delamination size shows strong dependence on assumed CE interface strengths, i.e. higher strength values cause reduction of delamination area (Fig. 18). This could potentially impact the residual strength of the laminate, since compression after impact is particularly sensitive to the size of delamination [42].

Table 4
Material properties for the OHT (IM7/8552) tests [61].

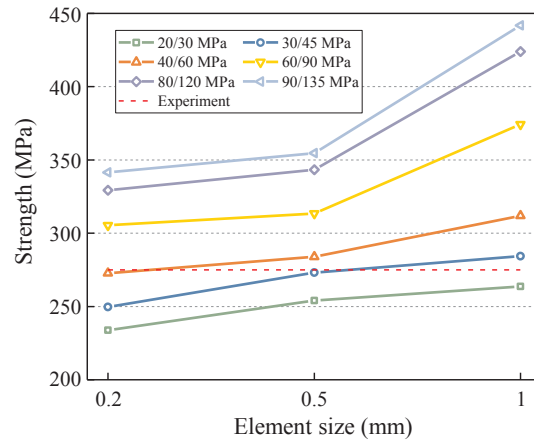| E_{11} (GPa)	E_{22}/E_{33} (GPa)	G_{12}/G_{13} (GPa)	G_{23} (GPa)	ν_{12}/ν_{13} (–)	ν_{23} (–)	G_{Ic}/G_{IIc} (N/mm)	τ_I^c/τ_{II}^c (MPa)	K_p (N/mm³)	α_{11} (°C⁻¹)	α_{22}/α_{33} (°C⁻¹)	ΔT (°C)
161	11.4	5.17	3.98	0.32	0.43	0.29/0.63	60/90	10^5	0	3×10^{-5}	160

Fig. 13. Predicted failure strengths with various interface strengths and element sizes.
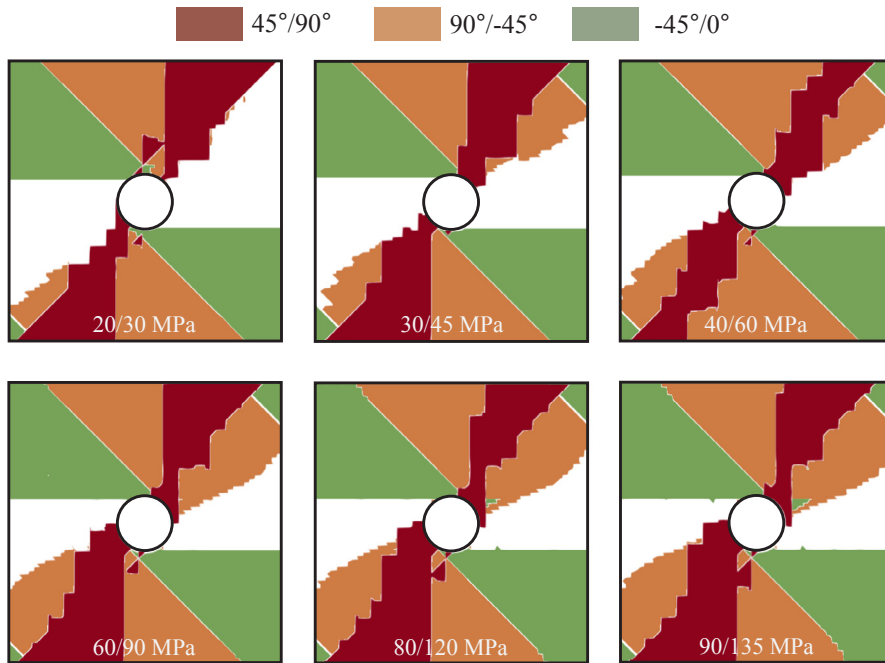

Fig. 14. Predicted delamination patterns (fully delaminated with damage factor = 1) right after load-drop with different interface strengths (0.2 mm mesh).

Remark 4 (*Interfacial strengths in structural failure process***).** Given the complex nature of composite laminated structures and the inherent interplay between various damage mechanisms among dissimilar plies, it is not always clear how the assumed strength values affect the progressive damage process and the predicted failure loads. For example, in OHT tests, varying the assumed CE strengths affects the predicted failure loads but delamination patterns remain relatively similar. On the other hand, in SI tests, the predicted loads do not exhibit much dependence on assumed CE strength values but the predicted delamination sizes are significantly affected.

Reducing CE strengths for the sake of computational efficiency, a strategy which has been successfully applied to fracture (strength-insensitive) tests [19], may not be directly applicable to structural damage analyses because the failure load becomes sensitive to the assumed cohesive strength values. Based on previous research and this work, artificial adjustment on interface strengths (either increase or reduce) is sometimes necessary to achieve accurate predictions in structural failure analyses. For the IM7/8552 OHT test in Section 3.5, if in-plane strengths are assumed for the interfacial values, significant overpredictions on the failure load are obtained. However, reducing the CE strengths results in better predictions compared to experiment.
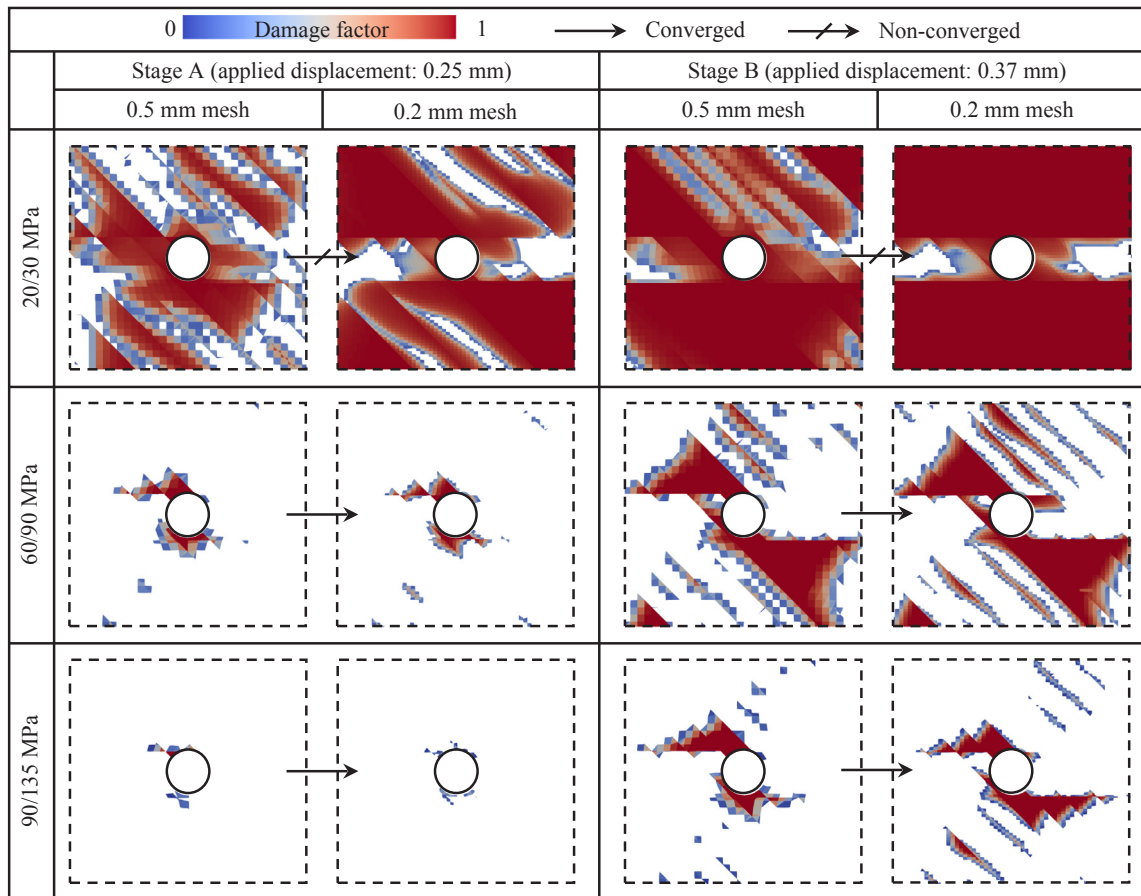
Engineering Fracture Mechanics 206 (2019) 278–296

Fig. 15. Comparison of the predicted interface damage at the $-45°/0°$ interface under the same applied displacement.

4. Penalty stiffness of a cohesive element

In this section, the influence of penalty stiffness K_p in delamination modelling with CEs is presented. The penalty stiffness of a zero-thickness CE should be sufficiently large to prevent spurious compliance resulting from the presence of the CEs but not too large to avoid numerical difficulties and high computational cost. Although the values of K_p commonly adopted for composite materials range from 10^4 to 10^8 N/mm^3 [31], they are not always reported in literature (Table 1).

There is apparently no universal criterion for selection of K_p values. Turon et al. proposed an empirical equation to determine the interface stiffness [19]:

$$K_p = \frac{\beta E_3}{t} \tag{9}$$

where t is the thickness of the adjacent sub-laminate and β is a parameter much larger than 1 ($\beta \gg 1$). A larger β is preferred to ensure that the compliance of the CE does not interfere with the overall compliance of the structure. Recently, Turon et al. [33–35] studied the effects of penalty stiffness in mixed-loading conditions and proposed a mode-dependent penalty stiffness for delamination. However, for simplicity we have used a constant mode-independent penalty stiffness in this present work. The influence of penalty stiffness on analysis results and computational efficiency is presented in the next sub-sections.

4.1. DCB and ENF analyses

The standard DCB and ENF models introduced in Section 3.2 are analysed with various assumed CE penalty stiffnesses. In the simulations, refined 0.1 mm meshes and fixed interfacial strengths (i.e., 57/90 MPa) are employed. The results for CE penalty stiffness K_p from 10^3 to 10^8 N/mm^3 are given in Fig. 19.

As shown in Fig. 19a and b, as long as the CE stiffness is larger than 10^4 N/mm^3, the loading responses obtained from both DCB and ENF tests are practically identical. The initial stiffness and the subsequent delamination propagation also agree with the analytical solution. Incorrect results are obtained in the extreme case of 10^3 N/mm^3. In fact, no propagation of delamination occurs because the peak stress in the CE could not be reached when $K_p = 10^3$ N/mm^3 is used. However, the number of iterations increases
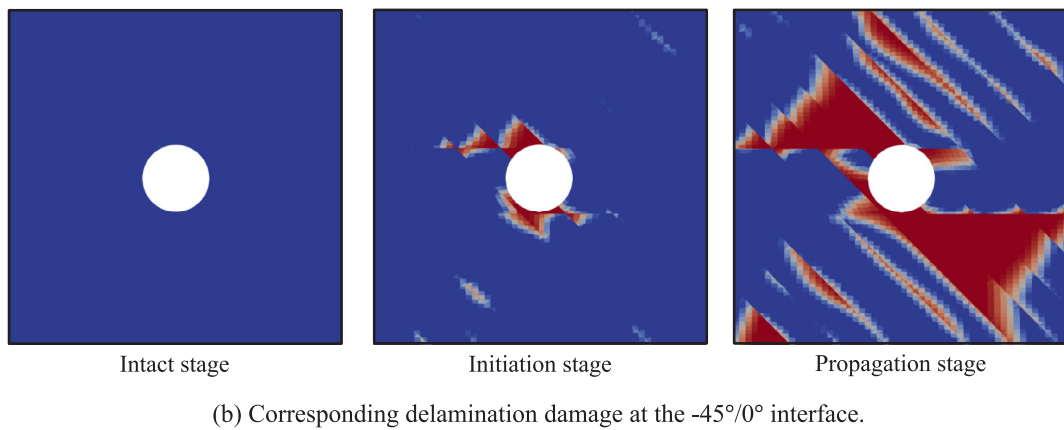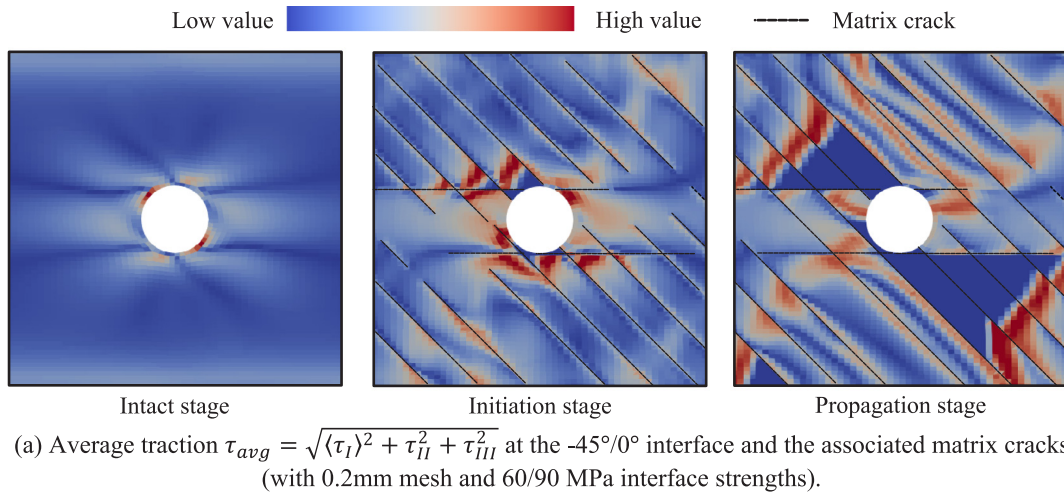
| Intact stage | Initiation stage | Propagation stage |

(a) Average traction $\tau_{avg} = \sqrt{\langle\tau_I\rangle^2 + \tau_{II}^2 + \tau_{III}^2}$ at the -45°/0° interface and the associated matrix cracks (with 0.2mm mesh and 60/90 MPa interface strengths).

| Intact stage | Initiation stage | Propagation stage |

(b) Corresponding delamination damage at the -45°/0° interface.

Fig. 16. Traction distribution and corresponding delamination damage at the $-45°/0°$ interface.

Table 5
Material properties for the SI (T700/M21) tests [41].

E_{11} (GPa)	E_{22}/E_{33} (GPa)	G_{12}/G_{13} (GPa)	G_{23} (GPa)	v_{12}/v_{13} (–)	v_{23} (–)	G_{Ic}/G_{IIc} (N/mm)	τ_I^c/τ_{II}^c (MPa)	K_p (N/mm^3)
130	7.7	4.8	3	0.33	0.4	0.6/2.1	60/110	10^6

dramatically when higher values of K_p are adopted (Fig. 19c and d). This is because higher K_p causes more oscillations in the Newton-Raphson scheme and in the extreme case, where K_p is excessively high, non-convergence can occur. Therefore, selecting an appropriate value of penalty stiffness strikes a balance between correctness of solution and computational efficiency. Unfortunately, there is currently no systematic way to do this other than by trial and error.

4.2. Structure-level tests

The OHT test (Fig. 12) is revisited in this section to study the influence of CE penalty stiffness in delamination analyses of complex composite structures. Based on previous discussions, reduced interfacial strengths (i.e., 30/45 MPa) and a 0.5 mm mesh are adopted. Penalty stiffnesses K_p varying from 10^4 to 10^8 N/mm^3 are applied in the models.

As shown in Table 6, if penalty stiffness values from 10^4 to 10^6 N/mm^3 are adopted, satisfactory predictions on the failure load are achieved when compared to experiment [98]. However, with higher K_p values, e.g. 10^7 and 10^8 N/mm^3, significant oscillations in the loading behaviour are observed during delamination propagation process, resulting in over-predictions of structural failure load. It is clear that the penalty stiffness has a strong impact on computational efficiency; the number of iterations increases with higher stiffness. It is noted that, from 10^4 to 10^7 N/mm^3, the iteration number increases by 185%, and convergence is not achieved for the case with the stiffness 10^8 N/mm^3.

As another example of structure-level analyses, the SI test in Section 3.6 (Fig. 17) is used for a parametric study on K_p. The
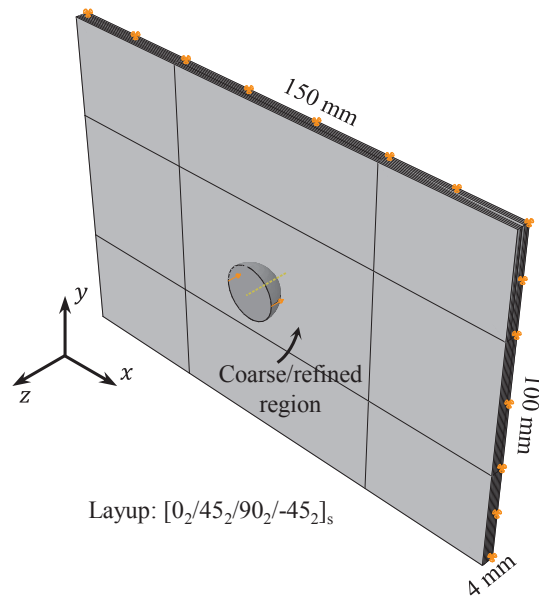
Fig. 17. Geometry and boundary conditions for static indentation (SI) test.
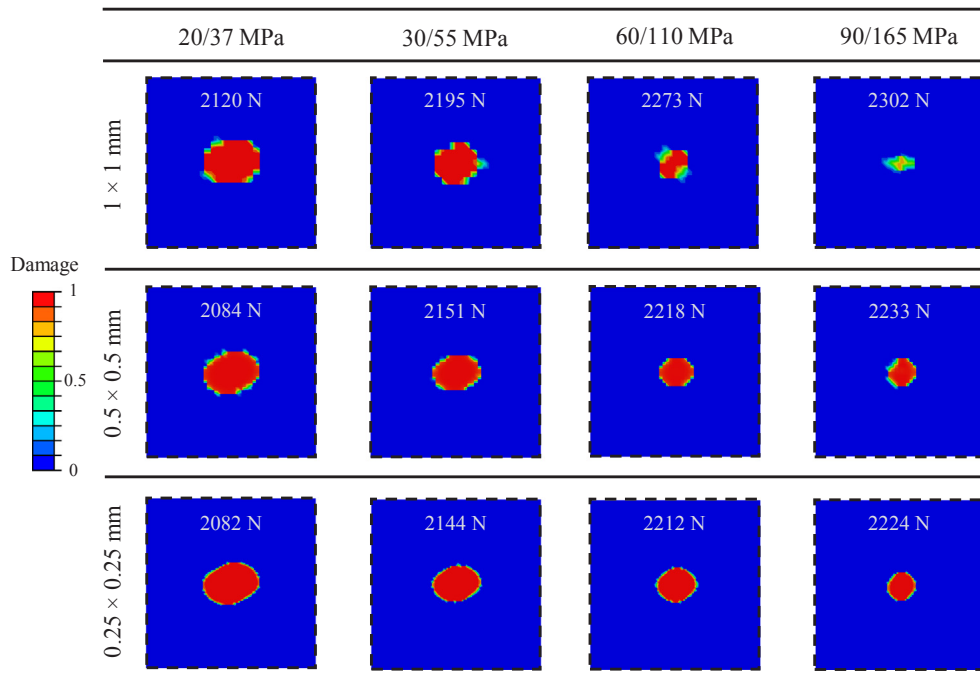

Fig. 18. Predicted delamination patterns at top 0°/45° interface and maximum indentation forces of static indentation (SI) test with different element sizes and interface strengths.

0.5×0.5 mm mesh and 60/110 MPa CE strengths are adopted, and K_p is varied from 10^4 to 10^8 N/mm^3.

The maximum indentation force and delamination pattern at the top 0°/45° interface are provided in Fig. 20. With K_p values larger than 10^5 N/mm^3, the penalty stiffness turns out to have limited influence on the load-displacement response and predicted delamination size. However, if stiffness values are too low, e.g. 10^4 N/mm^3, the predicted delamination becomes too small or disappears. In this case, the overall compliance is affected, with a decrease of 12% in the maximum load when compared to the case with $K_p = 10^8$ N/mm^3. The iteration number also increases by 953% when the K_p is raised from 10^5 to 10^8 N/mm^3.

Remark 5 (*Penalty stiffness in CE: The penalty stiffness plays a significant role in FE analyses*). The selection of a suitable K$_p$ value enables both accuracy and efficiency of simulation to be achieved. As observed in literature [30], the penalty stiffness shows little effect on
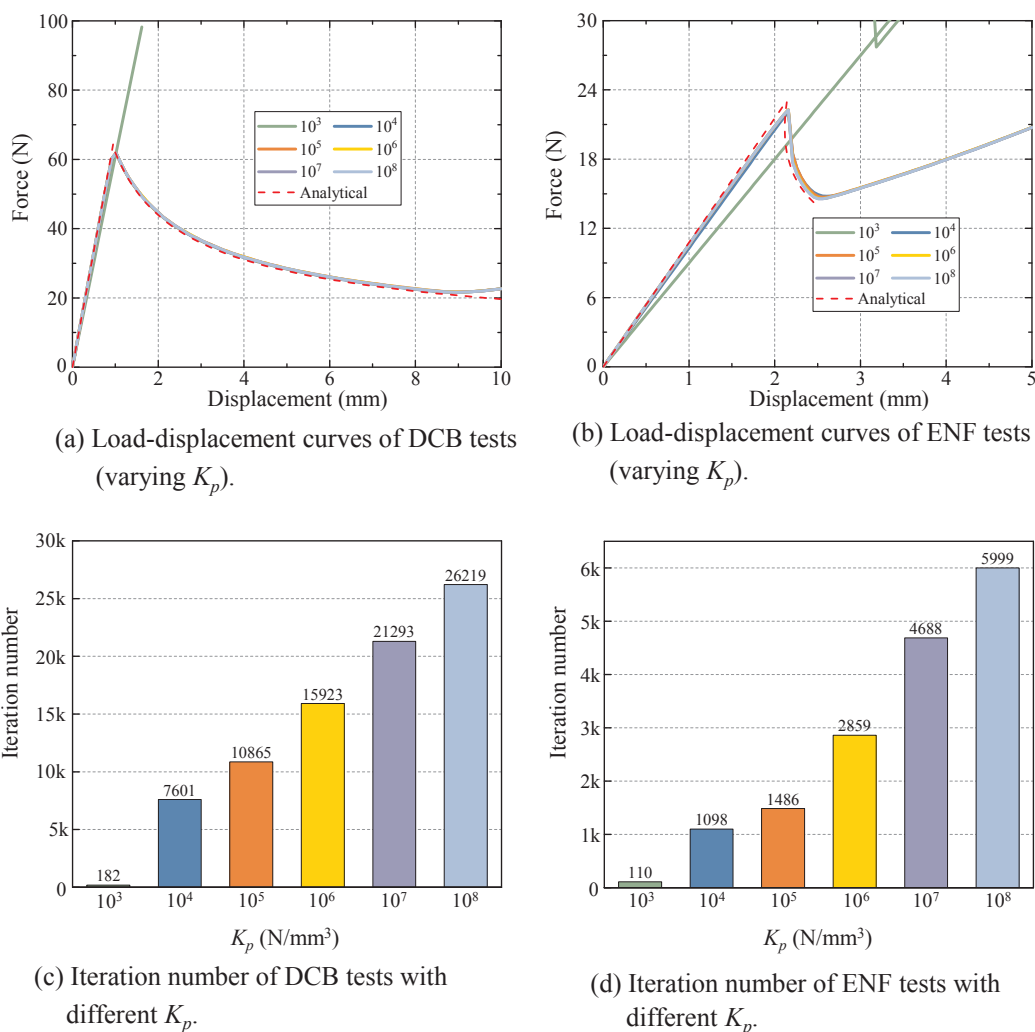
(a) Load-displacement curves of DCB tests (varying K_p).

(b) Load-displacement curves of ENF tests (varying K_p).

(c) Iteration number of DCB tests with different K_p.

(d) Iteration number of ENF tests with different K_p.

Fig. 19. Numerical results for DCB and ENF tests with different penalty stiffness K_p.

Table 6
Predicted failure strengths and total iteration numbers for OHT tests with different penalty stiffness values K_p (30/45 MPa interface strengths and 0.5 mm mesh).

Penalty stiffness (N/mm³)	10^4	10^5	10^6	10^7	10^8	Experiment [98]
Predicted failure load (N)	272	270	278	294[*]	308[*]	275
Iteration number	3747	4734	8208	10,703	35,643[**]	–

  * Significant oscillations in loading response have been observed during the delamination process, leading to inaccurate predictions.

  ** The simulation is terminated after the load drop due to excessively small time increment, and convergence is not expected.

the overall loading behaviour of the DCB and ENF specimens. However, its effects are greater for structural damage modelling where higher stiffness values are generally needed if no dominant cracks are present. Based on previous work [19,29] and the current study, penalty stiffness values of 10^5 to 10^6 N/mm³ are appropriate candidate choices for carbon/epoxy composites, allowing for both accuracy and feasibility of the simulation.

5. Conclusions

The effects of assumed cohesive element (CE) strengths and stiffnesses on delamination modelling are studied with coupon-level progressive damage analyses in the present paper. Due to difficulties in experimentally determining interfacial strengths of composites, assumed values are commonly adopted in delamination modelling with CEs. In problems where very high crack-like stress
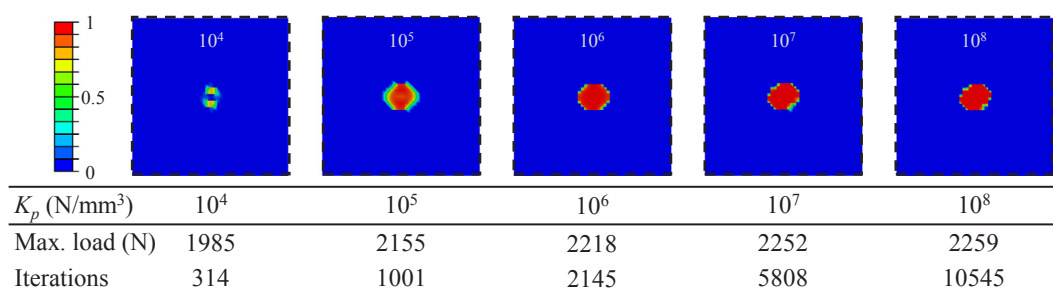
K_p (N/mm³)	10^4	10^5	10^6	10^7	10^8
Max. load (N)	1985	2155	2218	2252	2259
Iterations	314	1001	2145	5808	10545

Fig. 20. Numerical results for SI tests with different penalty stiffness K_p.

concentrations are present due to pre-existing cracks and sharp geometrical features, the results are relatively unaffected by assumed CE strengths, i.e. strength-insensitive. However, in composite structures where such high stress concentrators are not so obvious, the delamination fracture process significantly depends on the assumed CE strengths, i.e. strength-sensitive. In the latter case, it is acceptable to adopt ply material strength values as the CE interfacial strengths; however, adjusted values may be assumed for better predictive agreement with experiment, as demonstrated in analysis of open-hole tension (OHT) IM7/8552 laminates, in which reduced interface strengths have been applied.

The penalty stiffness K_p of CE also plays a significant role in delamination modelling. A stiffness that is too low leads to a model with artificially low overall structural stiffness and delayed damage initiation. High K_p values ensure correct representation of overall structural stiffness but at an expense of higher computational cost. An excessively high stiffness value leads to significant numerical oscillations and causes convergence difficulties. In most cases, a penalty stiffness ranging from 10^5 to 10^6 N/mm³ seems to be appropriate for carbon/epoxy laminates, for accuracy and efficiency.

Acknowledgement

References

[1] Tay TE. Characterization and analysis of delamination fracture in composites: an overview of developments from 1990 to 2001. Appl Mech Rev 2003;56:1–32.
[2] Schellekens JCJ, de Borst R. A non-linear finite element approach for the analysis of mode-I free edge delamination in composites. Int J Solids Struct 1993;30:1239–53.
[3] Corigliano A. Formulation, identification and use of interface models in the numerical analysis of composite delamination. Int J Solids Struct 1993;30:2779–811.
[4] Mi Y, Crisfield MA, Davies GAO, Hellweg HB. Progressive delamination using interface elements. J Compos Mater 1998;32:1246–72.
[5] Blackman BRK, Hadavinia H, Kinloch AJ, Williams JG. The use of a cohesive zone model to study the fracture of fibre composites and adhesively-bonded joints. Int J Fract 2003;119:25–46.
[6] Yang Q, Cox B. Cohesive models for damage evolution in laminated composites. Int J Fract 2005;133:107–37.
[7] Dugdale DS. Yielding of steel sheets containing slits. J Mech Phys Solids 1960;8:100–4.
[8] Barenblatt GI. The mathematical theory of equilibrium cracks in brittle fracture. Adv Appl Mech 1962;7:55–129.
[9] Park K, Paulino GH. Cohesive zone models: a critical review of traction-separation relationships across fracture surfaces. Appl Mech Rev 2011;64:060802.
[10] Alfano G. On the influence of the shape of the interface law on the application of cohesive-zone models. Compos Sci Technol 2006;66:723–30.
[11] Gutkin R, Laffan ML, Pinho ST, Robinson P, Curtis PT. Modelling the R-curve effect and its specimen-dependence. Int J Solids Struct 2011;48:1767–77.
[12] Park K, Paulino GH. Computational implementation of the PPR potential-based cohesive model in ABAQUS: educational perspective. Engng Fract Mech 2012;93:239–62.
[13] Shao Y, Zhao H-P, Feng X-Q, Gao H. Discontinuous crack-bridging model for fracture toughness analysis of nacre. J Mech Phys Solids 2012;60:1400–19.
[14] Reeder JR, Demarco K, Whitley KS. The use of doubler reinforcement in delamination toughness testing. Compos A Appl Sci Manuf 2004;35:1337–44.
[15] ASTM D5528-13 Standard test method for mode I interlaminar fracture toughness of unidirectional fiber-reinforced polymer matrix composites; 2013.
[16] ASTM D7905/D7905M-14 Standard test method for determination of the mode II interlaminar fracture toughness of unidirectional fiber-reinforced polymer matrix composites; 2014.
[17] ASTM D6671/D6671M-13e1 standard test method for mixed mode I-mode II interlaminar fracture toughness of unidirectional fiber reinforced polymer matrix composites; 2013.
[18] Alfano G, Crisfield MA. Finite element interface models for the delamination analysis of laminated composites: mechanical and computational issues. Int J Num Meth Eng 2001;50:1701–36.
[19] Turon A, Davila CG, Camanho PP, Costa J. An engineering solution for mesh size effects in the simulation of delamination using cohesive zone models. Eng Fract Mech 2007;74:1665–82.
[20] Harper PW, Hallett SR. Cohesive zone length in numerical simulations of composite delamination. Eng Fract Mech 2008;75:4774–92.
[21] Soto A, González E, Maimí P, Turon A, de Aja JS, de la Escalera F. Cohesive zone length of orthotropic materials undergoing delamination. Eng Fract Mech 2016;159:174–88.
[22] Parmigiani JP, Thouless MD. The effects of cohesive strength and toughness on mixed-mode delamination of beam-like geometries. Eng Fract Mech 2007;74:2675–99.
[23] Guiamatsia I, Ankersen J, Davies G, Iannucci L. Decohesion finite element with enriched basis functions for delamination. Compos Sci Technol 2009;69:2616–24.
[24] Samimi M, Van Dommelen J, Geers M. A three-dimensional self-adaptive cohesive zone model for interfacial delamination. Comput Meth Appl Mech Eng 2011;200:3540–53.
[25] Lu X, Chen BY, Tan VBC, Tay TE. Adaptive floating node method for modelling cohesive fracture of composite materials. Eng Fract Mech 2018;194:240–61.
[26] Harper PW, Sun L, Hallett SR. A study on the influence of cohesive zone interface element strength parameters on mixed mode behaviour. Compos A Appl Sci Manuf 2012;43:722–34.

[27] Daudeville L, Allix O, Ladevèze P. Delamination analysis by damage mechanics: some applications. Compos Eng 1995;5:17–24.

[28] Zou Z, Reid SR, Li S, Soden PD. Modelling interlaminar and intralaminar damage in filament-wound pipes under quasi-static indentation. J Compos Mater 2002;36:477–99.

[29] Camanho PP, Davila C, De Moura M. Numerical simulation of mixed-mode progressive delamination in composite materials. J Compos Mater 2003;37:1415–38.

[30] Yuan H, Li X. Effects of the cohesive law on ductile crack propagation simulation by using cohesive zone models. Eng Fract Mech 2014;126:1–11.

[31] Zhao L, Gong Y, Zhang J, Chen Y, Fei B. Simulation of delamination growth in multidirectional laminates under mode I and mixed mode I/II loadings using cohesive elements. Compos Struct 2014;116:509–22.

[32] Guo X, Zhang WJ, Zhu LL, Lu J. Mesh dependence of transverse cracking in laminated metals with nanograined interface layers. Eng Fract Mech 2013;105:211–20.

[33] Turon A, Camanho PP, Costa J, Renart J. Accurate simulation of delamination growth under mixed-mode loading using cohesive elements: definition of interlaminar strengths and elastic stiffness. Compos Struct 2010;92:1857–64.

[34] Sarrado C, Turon A, Renart J, Urresti I. Assessment of energy dissipation during mixed-mode delamination growth using cohesive zone models. Compos A Appl Sci Manuf 2012;43:2128–36.

[35] Turon A, González EV, Sarrado C, Guillamet G, Maimí P. Accurate simulation of delamination under mixed-mode loading using a cohesive model with a mode-dependent penalty stiffness. Compos Struct 2018;184:506–11.

[36] van der Meer FP, Sluys LJ. Mesh-independent modeling of both distributed and discrete matrix cracking in interaction with delamination in composites. Eng Fract Mech 2010;77:719–35.

[37] Higuchi R, Okabe T, Nagashima T. Numerical simulation of progressive damage and failure in composite laminates using XFEM/CZM coupled approach. Compos A Appl Sci Manuf 2017;95:197–207.

[38] Ridha M, Wang CH, Chen BY, Tay TE. Modelling complex progressive failure in notched composite laminates with varying sizes and stacking sequences. Compos A Appl Sci Manuf 2014;58:16–23.

[39] Su ZC, Tay TE, Ridha M, Chen BY. Progressive damage modeling of open-hole composite laminates under compression. Compos Struct 2015;122:507–17.

[40] Falcó O, Ávila RL, Tijs B, Lopes CS. Modelling and simulation methodology for unidirectional composite laminates in a Virtual Test Lab framework. Compos Struct 2018;190:137–59.

[41] Hongkarnjanakul N, Bouvet C, Rivallant S. Validation of low velocity impact modelling on different stacking sequences of CFRP laminates and influence of fibre failure. Compos Struct 2013;106:549–59.

[42] Abir MR, Tay TE, Ridha M, Lee HP. On the relationship between failure mechanism and compression after impact (CAI) strength in composites. Compos Struct 2017;182:242–50.

[43] Cui WC, Wisnom MR, Jones M. A comparison of failure criteria to predict delamination of unidirectional glass/epoxy specimens waisted through the thickness. Composites 1992;23:158–66.

[44] Benzeggagh ML, Kenane M. Measurement of mixed-mode delamination fracture toughness of unidirectional glass/epoxy composites with mixed-mode bending apparatus. Compos Sci Technol 1996;56:439–49.

[45] Turon A, Camanho PP, Costa J, Dávila C. A damage model for the simulation of delamination in advanced composites under variable-mode loading. Mech Mater 2006;38:1072–89.

[46] ASTM D3518/D3518M-13 Standard test method for in-plane shear response of polymer matrix composite materials by tensile test of a ± 45° laminate; 2013.

[47] ASTM D2344/D2344M-16 Standard test method for short-beam strength of polymer matrix composite materials and their laminates; 2016.

[48] ASTM D3039/D3039M-17 Standard test method for tensile properties of polymer matrix composite materials; 2017.

[49] Rice JR. A path independent integral and the approximate analysis of strain concentration by notches and cracks. J Appl Mech 1968;35:379–86.

[50] Sun CT, Jin ZH. Chapter 4 – energy release rate. In: Sun CT, Jin ZH, editors. Fracture mechanics. Boston: Academic Press; 2012. p. 77–103.

[51] Suo Z, Bao G, Fan B. Delamination R-curve phenomena due to damage. J Mech Phys Solids 1992;40:1–16.

[52] Sørensen BF, Jacobsen TK. Determination of cohesive laws by the J integral approach. Eng Fract Mech 2003;70:1841–58.

[53] Shet C, Chandra N. Effect of the shape of T–δ cohesive zone curves on the fracture response. Mech Adv Mater Struct 2004;11:249–75.

[54] Sørensen BF, Kirkegaard P. Determination of mixed mode cohesive laws. Eng Fract Mech 2006;73:2642–61.

[55] Högberg JL, Sørensen BF, Stigh U. Constitutive behaviour of mixed mode loaded adhesive layer. Int J Solids Struct 2007;44:8335–54.

[56] Sørensen BF, Goutianos S, Jacobsen TK. Strength scaling of adhesive joints in polymer–matrix composites. Int J Solids Struct 2009;46:741–61.

[57] Ji G, Ouyang Z, Li G, Ibekwe S, Pang S-S. Effects of adhesive thickness on global and local Mode-I interfacial fracture of bonded joints. Int J Solids Struct 2010;47:2445–58.

[58] Sarrado C, Turon A, Costa J, Renart J. An experimental analysis of the fracture behavior of composite bonded joints in terms of cohesive laws. Compos A Appl Sci Manuf 2016;90:234–42.

[59] Arrese A, Boyano A, De Gracia J, Mujika F. A novel procedure to determine the cohesive law in DCB tests. Compos Sci Technol 2017;152:76–84.

[60] Hallett SR, Jiang WG, Khan B, Wisnom MR. Modelling the interaction between matrix cracks and delamination damage in scaled quasi-isotropic specimens. Compos Sci Technol 2008;68:80–9.

[61] Hallett SR, Green BG, Jiang WG, Wisnom MR. An experimental and numerical investigation into the damage mechanisms in notched composites. Compos Part A: Appl Sci Manuf 2009;40:613–24.

[62] Fang XJ, Yang QD, Cox BN, Zhou ZQ. An augmented cohesive zone element for arbitrary crack coalescence and bifurcation in heterogeneous materials. Int J Num Meth Eng 2011;88:841–61.

[63] Iarve EV, Gurvich MR, Mollenhauer DH, Rose CA, Dávila CG. Mesh-independent matrix cracking and delamination modeling in laminated composites. Int J Num Meth Eng 2011;88:749–73.

[64] Iarve EV, Hoos KH, Nikishkov Y, Makeev A. Discrete damage modeling of static bearing failure in laminated composites. Compos Part A: Appl Sci Manuf 2018;108:30–40.

[65] Sun XC, Hallett SR. Failure mechanisms and damage evolution of laminated composites under compression after impact (CAI): experimental and numerical study. Compos A Appl Sci Manuf 2018;104:41–59.

[66] Ye Q, Chen P. Prediction of the cohesive strength for numerically simulating composite delamination via CZM-based FEM. Compos B Eng 2011;42:1076–83.

[67] van der Meer FP, Sluys LJ, Hallett SR, Wisnom MR. Computational modeling of complex failure mechanisms in laminates. J Compos Mater 2012;46:603–23.

[68] van der Meer FP. Mesolevel modeling of failure in composite laminates: constitutive, kinematic and algorithmic aspects. Arch Comput Meth Eng 2012;19:381–425.

[69] Chen BY, Tay TE, Baiz PM, Pinho ST. Numerical analysis of size effects on open-hole tensile composite laminates. Compos A Appl Sci Manuf 2013;47:52–62.

[70] Chen BY, Tay TE, Pinho ST, Tan VBC. Modelling the tensile failure of composites with the floating node method. Comput Meth Appl Mech Eng 2016;308:414–42.

[71] Lu X, Chen BY, Tan VBC, Tay TE. A separable cohesive element for modelling coupled failure in laminated composite materials. Compos A Appl Sci Manuf 2018;107:387–98.

[72] Topac OT, Gozluklu B, Gurses E, Coker D. Experimental and computational study of the damage process in CFRP composite beams under low-velocity impact. Compos A Appl Sci Manuf 2017;92:167–82.

[73] Zhi J, Chen B-Y, Tay T-E. Geometrically nonlinear analysis of matrix cracking and delamination in composites with floating node method. Comput Mech 2018.

[74] Fan C, Jar PYB, Cheng JJR. Cohesive zone with continuum damage properties for simulation of delamination development in fibre composites and failure of adhesive joints. Eng Fract Mech 2008;75:3866–80.

[75] Davila CG, Camanho PP. Analysis of the effects of residual strains and defects on skin/stiffener debonding using decohesion elements. 44th AIAA/ASME/ASCE/AHS/ASC structures, structural dynamics, and materials conference. American Institute of Aeronautics and Astronautics; 2003.

[76] Camanho PP, Maimí P, Dávila CG. Prediction of size effects in notched laminates using continuum damage mechanics. Compos Sci Technol 2007;67:2715–27.

[77] Swindeman MJ, Iarve EV, Brockman RA, Mollenhauer DH, Hallett SR. Strength prediction in open hole composite laminates by using discrete damage modeling.

AIAA J 2013;51:936–45.

[78] Wang CH, Gunnion AJ, Orifici AC, Rider A. Residual strength of composite laminates containing scarfed and straight-sided holes. Compos A Appl Sci Manuf 2011;42:1951–61.

[79] Zhou S, Sun Y, Chen BY, Tay TE. Material orthotropy effects on progressive damage analysis of open-hole composite laminates under tension. J Reinf Plast Compos. 2017;36:1473–86.

[80] De Carvalho N, Seshadri B, Ratcliffe J, Mabson G, Deobald L. Simulating matrix crack and delamination interaction in a clamped tapered beam; 2017.

[81] Chen BY, Tay TE, Pinho ST, Tan VBC. Modelling delamination migration in angle-ply laminates. Compos Sci Technol 2017;142:145–55.

[82] Hu XF, Lu X, Tay TE. Modelling delamination migration using virtual embedded cohesive elements formed through floating nodes. Compos Struct 2018;204:500–12.

[83] Ling DS, Fang XJ, Cox BN, Yang QD. Nonlinear fracture analysis of delamination crack jumps in laminated composites. J Aerosp Eng 2011;24:181–8.

[84] Hu XF, Chen BY, Tirvaudey M, Tan VBC, Tay TE. Integrated XFEM-CE analysis of delamination migration in multi-directional composite laminates. Compos A Appl Sci Manuf 2016;90:161–73.

[85] Tay T, Sun X, Tan V. Recent efforts toward modeling interactions of matrix cracks and delaminations: an integrated XFEM-CE approach. Adv Compos Mater 2014;23:391–408.

[86] Soto A, González EV, Maimí P, Mayugo JA, Pasquali PR, Camanho PP. A methodology to simulate low velocity impact and compression after impact in large composite stiffened panels. Compos Struct 2018;204:223–38.

[87] McElroy MW, Gutkin R, Pankow M. Interaction of delaminations and matrix cracks in a CFRP plate, Part II: Simulation using an enriched shell finite element model. Compos A Appl Sci Manuf 2017;103:252–62.

[88] Bouvet C, Rivallant S, Barrau JJ. Low velocity impact modeling in composite laminates capturing permanent indentation. Compos Sci Technol 2012;72:1977–2198.

[89] Zhou S, Sun Y, Muhammad R, Chen BY, Tay TE. Progressive damage simulation of scaling effects on open-hole composite laminates under compression. J Reinf Plast Compos 2017;36:1369–83.

[90] Hoos K, Iarve EV, Braginsky M, Zhou E, Mollenhauer DH. Static strength prediction in laminated composites by using discrete damage modeling. J Compos Mater 2016;51:1473–92.

[91] Yang QD, Schesser D, Niess M, Wright P, Mavrogordato MN, Sinclair I, et al. On crack initiation in notched, cross-plied polymer matrix composites. J Mech Phys Solids 2015;78:314–32.

[92] Yang QD, Cox BN, Nalla RK, Ritchie R. Fracture length scales in human cortical bone: the necessity of nonlinear fracture models. Biomaterials 2006;27:2095–113.

[93] Crossman FW, Wang ASD. The dependence of transverse cracking and delamination on ply thickness in graphite/epoxy laminates. In: Reifsnider KL, editor. Damage in composite materials: basic mechanisms, accumulation, tolerance, and characterization. ASTM International; 1982. p. 118–39.

[94] O'Brien TK. Characterization of delamination onset and growth in a composite laminate. In: Reifsnider KL, editor. Damage in composite materials: basic mechanisms, accumulation, tolerance, and characterization. ASTM International; 1982. p. 140–67.

[95] Pipes RB, Pagano NJ. Interlaminar stresses in composite laminates under uniform axial extension. J Compos Mater 1970;4:538–48.

[96] Pagano NJ. On the calculation of interlaminar normal stress in composite laminate. J Compos Mater 1974;8:65–81.

[97] Bertolini J, Castanié B, Barrau J-J, Navarro J-P. Multi-level experimental and numerical analysis of composite stiffener debonding. Part 1: non-specific specimen level. Compos Struct 2009;90:381–91.

[98] Green BG, Wisnom MR, Hallett SR. An experimental investigation into the tensile strength scaling of notched composites. Compos Part A: Appl Sci Manuf 2007;38:867–78.

[99] Panettieri E, Fanteria D, Danzi F. A sensitivity study on cohesive elements parameters: towards their effective use to predict delaminations in low-velocity impacts on composites. Compos Struct 2016;137:130–9.